journal of the mechanical behavior of biomedical materials 160 (2024) 106737

Contents lists available at ScienceDirect

Journal of the Mechanical Behavior of Biomedical Materials

journal homepage: www.elsevier.com/locate/jmbbm

Synthesis and evaluation of novel urethane macromonomers for the formulation of fracture tough 3D printable dental materials

Florian Schönl [a], Martin Demleitner [a], Jörg Angermann [b], Pascal Fässler [b], Iris Lamparth [b], Kai Rist [b], Thomas Schnur [b], Yohann Catel [b,**], Sabine Rosenfeldt [c], Holger Ruckdäschel [a,*]

[a] Department of Polymer Engineering, University of Bayreuth, Universitätsstr. 30, 95447, Bayreuth, Germany
[b] Ivoclar Vivadent AG, Bendererstrasse 2, 9494, Schaan, Principality of Liechtenstein
[c] Physical Chemistry I and Bavarian Polymer Institute, University of Bayreuth, Universitätsstr. 30, 95447, Bayreuth, Germany

ARTICLE INFO

Keywords:
UV-Curing
Dental materials
Methacrylates
Fracture toughness
Block copolymers
3D-printing

ABSTRACT

3D printing of materials which combine fracture toughness, high modulus and high strength is quite challenging. Most commercially available 3D printing resins contain a mixture of multifunctional (meth)acrylates. The resulting 3D printed materials are therefore brittle and not adapted for the preparation of denture bases. For this reason, this article focuses on toughening by incorporation of triblock copolymers in methacrylate-based materials. In a first step, three urethane dimethacrylates with various alkyl spacer length were synthesized in a one-pot two-step synthesis. Each monomer was combined with 2-phenoxyethyl methacrylate as a monofunctional monomer and a polycaprolactone-polydimethylsiloxane-polycaprolactone triblock copolymer was added as toughener. The formation of nanostructures via self-assembly was proven by small angle X-ray scattering (SAXS) and transmission electron microscopy (TEM). The addition of the triblock copolymer resulted in a strong increase in fracture toughness for all mixtures. The nature of the urethane dimethacrylate had a significant impact on fracture toughness and flexural strength and modulus of the cured materials. Most promising systems were also investigated via dynamic fatigue propagation da/dN measurements, confirming that the toughening also works under dynamic load. By carefully selecting the length of the urethane dimethacrylate spacer and the amount of block copolymer, materials with the desired physical properties could be efficiently formulated. Especially the formulation containing the medium alkyl spacer length (**DMA2**/PEMA) and 5 wt% **BCP1** (block copolymer), exhibits excellent mechanical properties and high fracture toughness.

1. Introduction

In the last few years, interest in additive manufacturing has grown for various industrial domains, due to its several advantages such as low amount of wasted material or high flexibility for product individualization. These factors make 3D printing not only optimal for prototyping, but also for products in the medical sector like prostheses. Additionally, 3D printing is an attractive technology, especially for dental applications, since it allows fast and cost effective manufacturing of customized dental materials (Andjela et al., 2022; Della Bona et al., 2021; Balhaddad et al., 2023; Punia et al., 2022; Cai et al., 2023; Tigmeanu et al., 2022). Moreover, the possibility to print several objects at once represents a considerable advantage. Digital light processing (DLP) and stereolithography (SLA) are the most commonly used 3D printing technologies in dentistry in order to produce various materials at high precision. These include tooth models, orthodontic appliances like splints and wax models for metal casting and press ceramics, as well as denture bases and teeth.

However, 3D printing of denture bases remains challenging until today (Altarazi et al., 2022; Aati et al., 2022; Falahchai et al., 2023). Especially as a combination of high fracture toughness with high flexural strength and modulus is required. Conventional denture bases, which are not made via 3D printing yet, are mainly made up of crosslinked polymethyl methacrylate (PMMA), and are typically prepared via thermal polymerization of methyl methacrylate (MMA)-based resin, which is obtained by mixing a powder and a liquid (Anusavice et al.,

* Corresponding author.
** Corresponding author.
E-mail addresses: yohann.catel@ivoclar.com (Y. Catel), holger.ruckdaeschel@uni-bayreuth.de (H. Ruckdäschel).

https://doi.org/10.1016/j.jmbbm.2024.106737
Received 16 May 2024; Received in revised form 6 September 2024; Accepted 8 September 2024
Available online 10 September 2024

2013; Krishna et al., 2015). The powder mainly comprises beads of PMMA and a thermal initiator (typically benzoyl peroxide), whereas the liquid is mainly made up of MMA, small amount of dimethacrylates, and additives (inhibitors, etc.). Due to its high volatility and low reactivity, MMA is unfortunately not suitable for 3D printing. Therefore, current 3D printing resins in the dental industry are typically based on a mixture of highly reactive multifunctional (meth)acrylates. Their polymerization results in the formation of highly crosslinked, brittle networks that do not fulfill the requirements of denture base materials. In terms of conventionally used systems, one example is the material "ProBase Hot". This via heat curable system shows a fracture toughness (K_{IC}) of 1.44 ± 0.18 MPa$\sqrt{m}$ and a work of fracture (W_f) of 270 ± 30 J/m^2 (Zappini et al., 2003). Furthermore, a study from Geiger et al. shows a comparison of commercially available resin systems for the use as denture bases. Here, all four materials a suitable for 3D printing via DLP. The tested systems exhibit fractures toughness values in a range from 0.71 MPa$\sqrt{m}$ to 0.98 MPa$\sqrt{m}$ and a work of fracture in a range from 49.6 J/m^2 to 95.4 J/m^2. This shows that commercially available systems on the market can't yet compete with conventional systems and efficient toughening technologies are needed (Geiger et al., 2024).

Several techniques have already been used in literature to significantly increase the fracture toughness of polymer networks (Ligon et al., 2016; Wang et al., 2019). Most studies deal with the toughening of brittle epoxy networks (Utaloff et al., 2019; Mi et al., 2022). The addition of reactive rubbers such as carboxy terminated butadiene acrylonitrile copolymers, (Bagheri et al., 2009) core-shell particles, (Mousavi et al., 2021) block copolymers (BCPs), (Ruiz-Pérez et al., 2008) thermoplastic particles, (Hodgkin et al., 1998) hyperbranched polymers, (Santiago and Serra, 2022) silica nanoparticles (Sprenger, 2020) or polyhedral oligomeric silsesquioxane (POSS) (Mishra et al., 2017) to epoxy resins efficiently led to an increased fracture toughness.

First groundbreaking work in regards to toughening via the incorporation of BCPs was performed by Bates et al. and represented a major breakthrough (Hillmyer et al., 1997; Lipic et al., 1998). Indeed, this approach significantly improves fracture toughness without strongly impairing the flexural modulus and the glass transition temperature (T_g) of the cured epoxy resins. This efficient toughening effect is due to the formation of nanostructures, which can be formed either through self-assembly or reaction-induced microphase separation (RIMPS) (Cong et al., 2014). Here, self-assembly is based on the incorporation of amphiphilic diblock or triblock copolymers to epoxy resins, which contain "epoxy-philic" and "epoxy-phobic" blocks. Key parameters such as the nature of the blocks, molecular weight or block length as well as parameters for block-block and block-matrix interaction of the BCPs define their final structure via self-assembly which leads to the formation of distinct micro- or nanostructures in the forms of spherical or worm-like micelles or vesicles (Wu et al., 2005; Dean et al., 2001, 2003; Kishi et al., 2015; Ritzenthaler et al., 2002). The formed nanostructures are fixed in the material after curing. In the case of nanostructures generated via reaction-induced microphase separation mechanism, each block of the BCP is initially miscible in the matrix. The nanostructures are generated during the curing reaction of the epoxy matrix due to the microphase separation of a part of subchains of the BCPs (Meng et al., 2006a, 2006b; Xu et al., 2016). The main toughening mechanism of BCP-containing epoxy resin is particle cavitation followed by matrix shear banding.

Contrary to epoxy materials, only a few articles have been published regarding toughening of dimethacrylate networks. Roshanali et al. (2020) as well as Sandmann et al. (2015) reported the toughening of such networks via the use of core-shell particles (CSPs). In both cases, only a moderate improvement of the fracture toughness was noticed. Redline et al. tried to improve the fracture toughness of bis-glycidyl methacrylate (GMA) based networks via the incorporation of a poly (ethylene-alt-propylene)-b-poly(ethylene oxide) diblock copolymer (Redline et al., 2011). Although the formation of spherical micelles via self-assembly was clearly observed, the increase in fracture resistance was modest. Thus, the well-known toughening concepts used for epoxy materials are rather inefficient in highly crosslinked di(meth)acrylate networks. This phenomenon is likely caused by the inherent inhomogeneity of the networks obtained via radical polymerization of di (meth)acrylates.

Interestingly, it was reported that the toughening efficiency of BCPs in epoxy materials can be improved by lowering the crosslink density of the network (Thompson et al., 2009). Demleitner et al. adapted this concept to methacrylate-based materials and showed that dimethacrylate networks exhibiting low crosslink density can be successfully toughened with a polycaprolactone-polydimethylsiloxane-polycaprolactone (PCL-PDMS-PCL) BCP (Demleitner et al., 2022). Nanostructures were efficiently formed via self-assembly of the BCP in the resin. Such networks were prepared via the copolymerization of a urethane dimethacrylate macromonomer and of a monofunctional methacrylate. It has been clearly demonstrated that the higher the amount of the monofunctional monomer, the better the toughness. The increase of fracture toughness was significant. The formulated resins exhibited high reactivity and low viscosity and were suitable for 3D printing application.

In addition to the increase in fracture toughness under static load, the influence of dynamic load on fracture toughness must also be considered. Though, way less studies are known in the field of (meth)acrylate-based systems, most of which only deal with PMMA systems (Bucknall and Dumpleton, 1987) or investigate commercially available dental material systems (Shah et al., 2009). More in-depth investigations with regard to dynamic fatigue crack propagation (FCP) da/dN measurements can mainly be found in the direction of thermoplastic blend systems (Ruckdäschel et al., 2007, 2008), as well as for epoxy resin systems via the use of rigid particles like nano silica (Kothmann et al., 2015, 2017) or BCPs (Hübner et al., 2021).

As already mentioned, denture bases must exhibit a combination of high fracture toughness combined with high flexural strength and modulus. Obviously, it is expected that the nature of the urethane dimethacrylate will strongly influence these properties of the cured resins. The physical properties of the BCP-based materials could therefore be further improved by the modification of the crosslinker. Therefore, the main goal of the present study is to develop a basic understanding of the influence of the chosen materials in regard to their toughening potential. This first step is important to understand the general effects that a potential toughening of methacrylates with blockcopolymers might have. All individual material components were selected specifically with regard to their basic suitability for use in 3D printing. This allows for future in depth studies to transfer the gained knowledge to 3D printing itself.

In the present study, urethane dimethacrylates **DMAs 1**–**3** (Fig. 1) are synthesized and evaluated as crosslinking monomers in a matrix that additionally contains 2-phenoxyethyl methacrylate (PEMA) as monofunctional monomer and a PCL-PDMS-PCL **BCP1** (**BCP1** = **Block Copolymer 1**) as toughening agent. The structure of **DMAs 1**–**3** differs in the length of the alkyl group between the urethane moieties. Here, DMA1 has the longest spacer with 10 repeating alkyl groups, while DMA3 has the shortest spacer with only 2 repeating alkyl groups. The influence of the spacer length on the flexural strength, flexural modulus, glass transition temperature (T_g), and fracture toughness of the **BCP**-modified networks will be discussed.

2. Materials and methods

2.1. Materials

3-Isocyanatomethyl-3,5,5-trimethylcyclohexyl-isocyanate (IPDI) was purchased from TCI and 2-hydroxyethylmethacrylate (HEMA) from Nordmann Switzerland AG. Dibutyltin dilaurate (DBTDL) and 1,2-ethanediol were obtained from Brenntag Schweizerhall AG. 1,6-Hexanediol was purchased from Merck KGaA and the initiator Genocure TPO

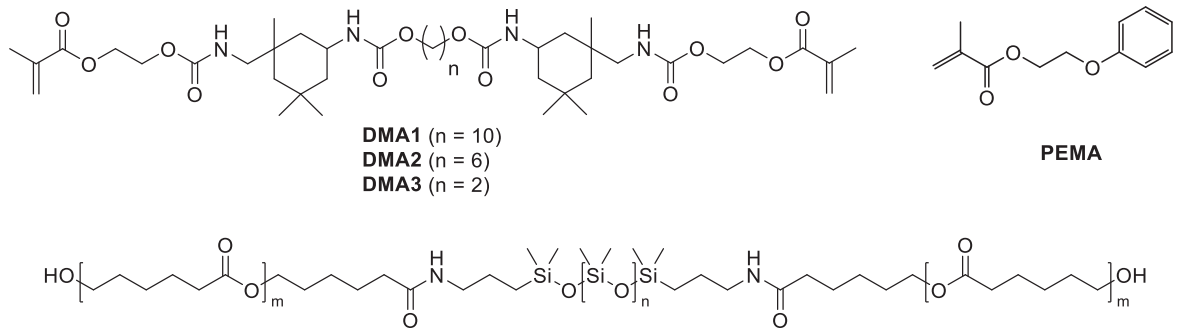

Fig. 1. Structures of **DMAs 1**–**3**, PEMA and **BCP1**.

((2,4,6-Trimethylbenzoyl)diphenylphosphine oxide) by Rahn AG. 2-Phenoxyethyl methacrylate (PEMA) was purchased from Sartomer (France) and was used as received. 2,6-Di-tert-butyl-4-methylphenol (BHT) was purchased from Sigma-Aldrich. **DMA1** and **BCP1** were synthesized according to the literature from the previous work of the authors (Demleitner et al., 2022).

2.2. Preparation of the formulations

Dimethacrylates **DMAs 1**–**3** and PEMA were used in weight ratios of 50/50 (as well as 30/70 for reactivity measurements). **BCP1** was added in various concentrations (3, 5 and 10 wt%). 1 mol% TPO was used as photoinitiator. **BCP1** and TPO were added to the **DMAs 1**–**3**/PEMA resins and the mixtures were heated to 50 °C until a clear solution was obtained.

2.3. Measurement methods and characterization

2.3.1. Nuclear magnetic resonance spectroscopy (NMR)

Nuclear magnetic resonance (NMR) analysis was conducted using a DPX-400 spectrometer from Bruker Biospin, with deuterated chloroform ($CDCl_3$) as the solvent. The results are presented with the chemical shifts in parts per million (ppm), followed by multiplicity indicators (brs for broad singlet, s for singlet, m for multiplet), and assignment (see supplementary information).

2.3.2. Infrared spectroscopy (IR)

IR spectroscopy was conducted using a PerkinElmer FT-IR Spectrum Two (UATR Two) spectrometer.

2.3.3. Photopolymerization procedure

Photopolymerizations were conducted utilizing a PerkinElmer Pyris Diamond differential scanning calorimeter (DSC). Each mixture was supplemented with 1.0 mol% TPO as the photoinitiator. The experiments were carried out under nitrogen atmosphere (20.0 ml/min). A mass of 1.0 mg was used for all mixtures and placed in an uncovered aluminum DSC pan. Prior to data acquisition, the DSC chamber was purged for 4 min via nitrogen. After 1 min, the samples were irradiated for 2 min at 37 °C using an LED UV-lamp (with peak intensity at 400 nm, from Ivoclar Vivadent AG). The irradiation intensity was set to 20 mW/cm^2. The experiments were repeated three times and monitoring of the heat flux took place under isothermal conditions. Double-bond conversion (DBC) was determined by calculating the ratio between the overall evolved enthalpy [ΔH_P (J g^{-1})] and the theoretical enthalpy expected for 100 % conversion of the mixtures [ΔH_{0P} (J g^{-1})] (equation (1)).

$$DBC = \frac{\Delta H_p}{\Delta H_{0p}} \tag{1}$$

ΔH_{0P} was calculated according to the following formula (equation (2))

$$\Delta H_{0p} = \Sigma\ \Delta H_{0i}.P_i/M_i \tag{2}$$

where ΔH_{0i} is the theoretical reaction enthalpy of monomer i (i = monomethacrylate, ΔH_{0i} = 54.8 kJ mol^{-1}; (Anseth et al., 1994) i = dimethacrylate, ΔH_{0i} = 109.6 kJ mol^{-1}), M_i its molar mass and P_i the amount used in the formulation by weight. The polymerization rate (R_p) was determined using the formula provided below (equation (3)):

$$R_p = Q/(m\ .\Delta H_{0P}) \tag{3}$$

Here, Q represents the heat flow per second during the reaction, and m stands for the mass of the mixture in the sample.

2.3.4. Dynamic-mechanical-thermal analysis (DMTA)

The DMA specimens were prepared using a stainless-steel mold (50 x 10 × 2 mm^3) with a polyester film (50 μm) as cover to avoid oxygen inhibition. After light-curing for 90 s from both sides in a PrograPrint Cure LED curing unit (120 mW/cm^2 at a wavelength of 405 nm), specimens were removed from the mold. A heating rate of 3 K/min in torsional mode, deformation of 0.1 % and a frequency of 1 Hz (Rheometrics Scientific ARES RDA III, Germany) based on DIN EN ISO 6721-2 were used. The glass transition temperature (T_g) was determined using the peak of the loss factor tan δ. Additionally, the DMTA measurements give access to the storage modulus E'. This value can be calculated by

$$E' = 2 \bullet (1 + \nu) \bullet G' \tag{4}$$

where ν stands for the Poisson ratio, where 0.37 of PMMA was used. (Bhushan and Burton, 2005) G' describes the value of the storage shear modulus at room temperature.

2.3.5. Flexural strength and modulus

Specimens (2 x 2 × 25 mm^3) were prepared via the use of a stainless-steel mold. The mold was filled with the monomer mixture and covered with a polyethylene film. After light-curing for 90 s from both sides in a PrograPrint Cure LED curing unit (120 mW/cm^2 at a wavelength of 405 nm), the specimens were stored in water at 37 °C for 24 h after removal from the mold. Flexural strength and modulus were determined through three-point bending tests (with a span width of 20 mm) conducted at a speed of 0.8 mm/min, employing a Z2.5/TS universal testing machine (Zwick, Germany), according to ISO4049:2019.

2.3.6. Fracture toughness K_{IC} and critical energy release rate G_{IC}

Fracture toughness determination was carried out via critical stress intensity factor (K_{IC}-value) under tensile opening mode (mode I), following the guidelines specified in ISO 13586 (Specimen dimensions: 42,25 x 39,6 × 5 mm^3). Testing was performed using a Zwick Z050 universal testing machine (Zwick Roell, Ulm, Germany), employing compact tension (CT) specimens. First crack initiation was performed

using a sharp razor blade. Test parameters included an initial load of 1 N and 10 mm/min as testing speed and at least 5 samples were tested each. After testing the exact crack length was measured. The fracture toughness at crack initiation, as well as the critical stress intensity factor K_{IC}, were calculated using the equation provided below:

$$K_{IC} = \frac{F_m}{t\sqrt{w}} \bullet f\left(\frac{a}{w}\right) \quad (5)$$

Here, F_m represents the maximum load at failure, t the thickness of the sample, w the overall length, a the crack length, and $f(a/w)$ a geometry factor according to ISO 13586 standards.

Furthermore, the critical energy release rate G_{IC} was determined using the equation:

$$G_{IC} = \frac{K_{IC}^2}{E} \bullet (1 - \nu^2) \quad (6)$$

where E stands for the modulus of elasticity taken from the DMTA measurements, and ν represents the Poisson ratio, using 0.37 for MMA systems based on literature. (Bhushan and Burton, 2005) To avoid potential effects of ageing, testing was carried out within 24 h after sample preparation.

2.3.7. Scanning electron microscopy (SEM)

The fracture mechanisms were analyzed using the K_{IC} samples after testing, using a Zeiss Leo 1530 scanning electron microscope (Carl Zeiss AG, Oberkochen, Germany) operating at an accelerating voltage of 3 kV. Prior to SEM observations, the specimens were coated with platinum (with an approximate thickness of ~1.5 nm) using a sputter coater.

2.3.8. Transmission electron microscopy (TEM)

Specimens were prepared using a diamond knife (Ultramikrotom Leica Model UC7) at room temperature. Subsequently, the samples underwent RuO_4 staining for 15 min. TEM measurements were conducted utilizing a Zeiss LEO EM922 Ω TM field emission energy filtering transmission electron microscope (FE-EFTEM) with an acceleration voltage of 200 kV. Zero-loss filtered micrographs (ΔE ~ 0 eV) were captured using a bottom-mounted CMOS camera system (OneView, Gatan) and further processed via DM 3.3 image processing software (Gatan).

2.3.9. Small-angle X-ray scattering (SAXS)

For measurements, the samples were filled in glass tubes (Hildenberg GmbH, code-no. 4007610 or 4007805). SAXS experiments were performed by a lab-based Double Ganesha AIR system (SAXSLAB/Xenocs) equipped with a copper rotating anode (MicroMax 007HF, Rigaku Corporation Japan, wavelength λ = 1.54 Å) and a PILATUS 300K detector (Dectris). Data reduction and azimuthal integrations were performed with the software provided by the instrument. For further evaluation the software SasView (Version 4.2.2) was used (Doucet et al., 2019).

2.3.10. Compression testing and calculation of plastic zone

Compression tests were conducted using a Z050 universal testing machine from ZwickRoell GmbH & Co. KG, Germany, equipped with a 20 kN load cell and operating at a crosshead speed of 1 mm/min. At least five samples, each with dimensions of 10 × 10 × 4 mm^3, according to DIN EN ISO 604 standard were tested. The compressive yield strength was identified by the lowest slope on the stress-strain curve. Additionally, to quantify the materials brittleness, the radius of the plastic zone (r_p) within the ligament was calculated based on Irwin's theory, assuming plane-strain deformation via the following formula

$$r_p = \frac{1}{6\pi}\left(\frac{K_{IC}}{\sigma_y}\right)^2 \quad (7)$$

where K_{IC} is the critical stress intensity factor and σ_y the compressive yield stress. (Broek, 1982; Grellmann and Seilder, 2013)

2.3.11. Dynamic fatigue crack propagation (da/dN)

Fatigue crack propagation (FCP) experiments were conducted at a temperature of 23 °C and 50 % relative humidity using a computer-controlled servo-hydraulic testing machine (Hydropuls MHF, Schenck) based on ISO 15850/ASTM E647 standards. Compact-tension (CT) specimens, matching the dimensions from K_{IC} testing, were used for the FCP testing. First crack initiation occurred by subjecting samples to a low sinusoidal load. To ensure reproducibility, a minimum of three specimens were tested, all displaying consistent results in strong agreement with each other. A thorough overview of the principle on the method can be found in literature (Kothmann, 2017; Abou and Jaoude, 2015). Fig. 2 shows the 3 different phases of crack propagation during dynamic testing, showcased with a direct example from the measurements used in the present study.

Herein the crack growth rate da/dN can be described with Paris and Erdogan law

$$\frac{da}{dN} = C\Delta K^m \quad (8)$$

where a describes the crack length, N the number of cycles and ΔK the stress intensity factor. C describes the material parameter, in detail the fatigue crack growth rate constant under cyclic loading and m the slope within the Paris Law of region 2. (Abou and Jaoude, 2015)

2.4. Synthesis of DMA2 and DMA3

A mixture of 1 eq. diol, 2 eq. IPDI and 700 ppm (based on IPDI) of DBTDL was heated to 40 °C. Complete dissolution of the diol occurred, resulting in a temperature rise to approximately 110 °C. Following the subsiding of the exothermic reaction, the mixture was stirred for 1 h at 80 °C before adding 2 eq. of HEMA. Subsequently, the mixture was stirred for 10 min at 90 °C, with the total consumption of isocyanate monitored using IR and NMR spectroscopy. **DMA2** and **DMA3** were obtained in quantitative yields as colorless highly viscous oils.

DMA2:

See supplementary information for detailed characterization.

DMA3:

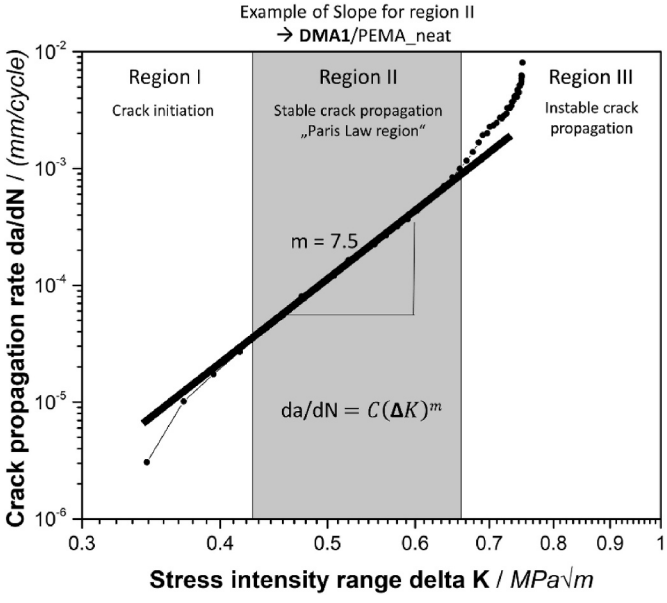

Fig. 2. Overview of the 3 different phases of crack propagation during dynamic load as a direct example from the present study.

See supplementary information for detailed characterization.

3. Results and discussion

3.1. Synthesis and reactivity of urethane monomers

DMA2 and **DMA3** were synthesized according to the procedure of **DMA1** using the corresponding diols. A detailed description of synthesis and their complete characterization by NMR and IR is available in the supporting information Fig. 3 shows the synthesis process.

The reactivity of urethane monomers **DMAs 1–3** was investigated using a photo-DSC. Due to the high viscosity of **DMAs 1–3**, their homopolymerization could not be performed. Therefore, co-polymerizations with PEMA were carried out. Two different ratios by weight were considered: **DMAs 1–3**/PEMA with 50/50 wt% and 30/70 wt%. 1.0 mol% TPO was used as photoinitiator and irradiation occurred for 2 min at 37 °C (using an LED UV-lamp with a maximum intensity at 400 nm and irradiation intensity of 20 mW/cm^2). Homopolymerization of PEMA was also carried out. Figs. 4 and 5 represent the rate of polymerization (R_p) and the double bond conversion (DBC) as a function of time, respectively.

As expected, the addition of **DMAs 1–3** to PEMA led to a significant increase of the reactivity. The higher the amount of dimethacrylate, the faster the polymerization and the lower the DBC. Indeed, a strong decrease of the time to reach the maximum rate of polymerization (t_{Rpmax}) is observed upon addition of **DMAs 1–3**. **DMAs 1–3** are cross-linking monomers. The photopolymerization of **DMAs 1–3**/PEMA mixtures therefore results in the formation of networks. The decrease of the DBC is clearly due to a decrease of the radicals mobility. The higher the content of crosslinker, the higher the crosslink density and the lower the mobility of radicals. It has been reported that the presence of urethane groups, due to the formation of hydrogen bonds, results in a strong increase of the reactivity of (meth)acrylate monomers (Cramer et al., 2008; Berchtold et al., 2004). It can thus be assumed that the presence of the four urethane groups plays a significant role on the excellent reactivity of **DMAs 1–3**.

The results also show that the nature of the **DMA** spacer has a significant influence on both the polymerization rate and the DBC. Indeed, the longer the alkyl spacer, the lower the reactivity (higher t_{Rpmax} values) and the higher the DBC. This trend is again related to a difference in radicals mobility (the longer the flexible spacer, the higher the mobility).

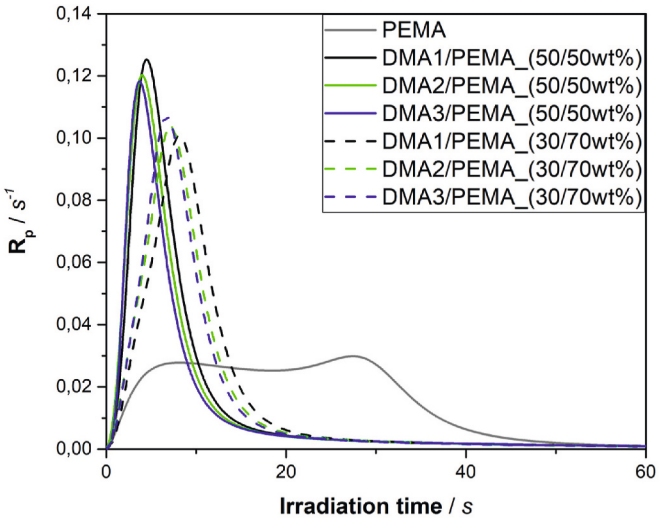

Fig. 4. R_p versus irradiation time for the copolymerization of monomers **DMAs 1–3** with PEMA using TPO (1.0 mol%) as photoinitiator.

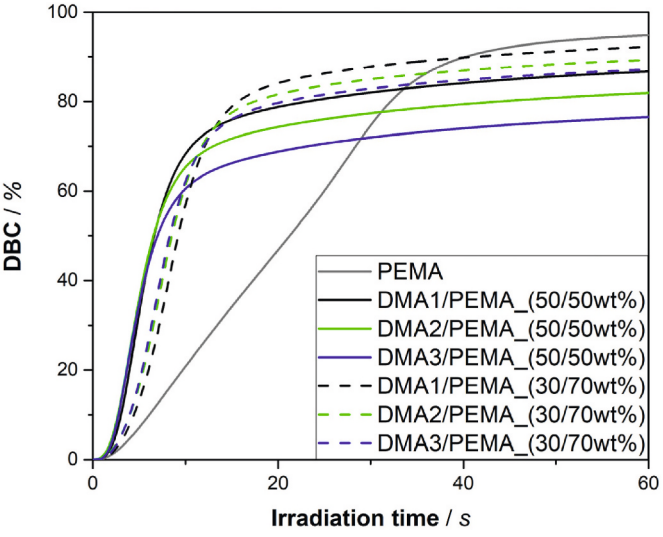

Fig. 5. DBC versus irradiation time for the copolymerization of monomers **DMAs 1–3** with PEMA using TPO (1.0 mol%) as photoinitiator.

3.2. DMTA analysis and mechanical properties (flexural strength and modulus) of DMAs 1–3 based materials

Following the technology that was recently developed for the formulation of fracture-tough dimethacrylate-based materials (Demleitner et al., 2022), **DMAs 1–3** were firstly mixed with PEMA (**DMAs 1–3**/PEMA: 50/50 wt/wt) and TPO was added as photoinitiator. The presence of the monofunctional methacrylate is essential to significantly reduce the network density of the cured materials and therefore to improve the toughening ability. For each of these mixtures, 0, 3, 5 and 10 wt% of **BCP1** were added. This triblock copolymer (PCL (1600 g/mol) – PDMS (3200 g/mol) -PCL (1600 g/mol)) was recently identified as a highly efficient toughening agent for low crosslink density methacrylate networks (Demleitner et al., 2022). Each monomer mixture was then cured using a PrograPrint Cure LED light-curing unit. The T_g of the resulting networks was measured using DMTA (see Table 1). Here, information on the storage shear modulus G' and T_g could be obtained. Fig. 6 shows exemplarily an overview of the storage modulus and tan δ for the **DMA3**/PEMA systems.

The results show that for each **DMA**/PEMA mixture, an increase of the **BCP1** content leads to a decrease of the storage modulus (with exaptation of **DMA3**/PEMA with 3% and 5% **BCP1** showing similar values for G′, and consequently for E', see Table 1). Due to the inclusion of the **BCP1** toughener, it is expected that the network density within the systems decreases by increasing the **BCP1** content due to steric

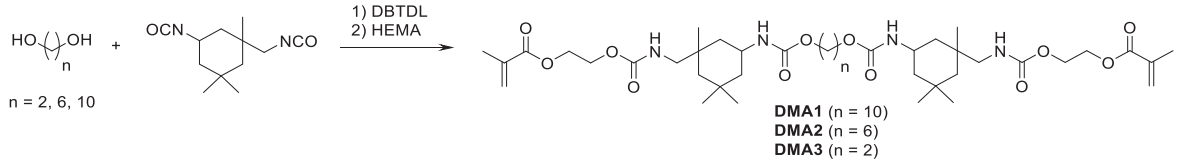

Fig. 3. Synthesis of the urethane monomers **DMAs 1–3**.

Table 1
Overview of the results of the DMTA measurements of the **DMAs 1**–**3**/PEMA systems including the variation of the **BCP1** toughener.

System	BCP1/wt%	G'/MPa	E'/MPa	T_g/°C
DMA1/PEMA	0	1057	2876	87
	3	1049	2854	85
	5	1019	2772	85
	10	889	2417	84
DMA2/PEMA	0	1124	3056	94
	3	1086	2952	91
	5	1020	2774	92
	10	915	2489	92
DMA3/PEMA	0	1317	3581	105
	3	1245	3385	103
	5	1256	3416	102
	10	1090	2964	102

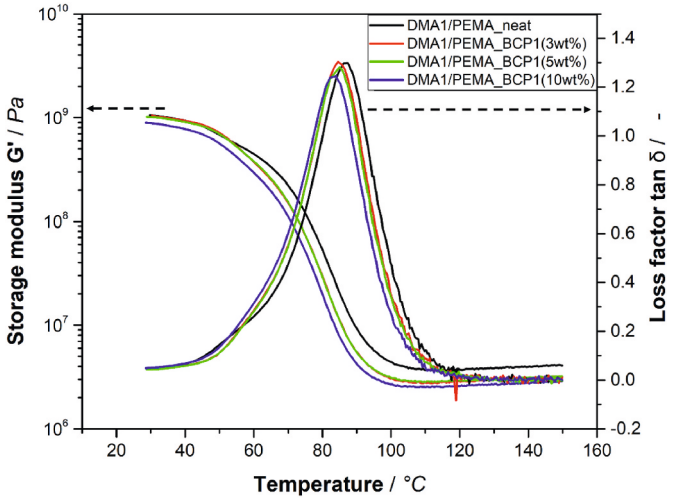

Fig. 6. Storage modulus and tan δ for the **DMA3**/PEMA mixtures.

hindrance of the incorporated particles. At the same time, the elastic particles, formed by aggregation of PDMS-blocks due to the self-organization of **BCP1**, exhibit a significantly lower modulus and have consequently a negative effect on the modulus of the overall system.

Interestingly the incorporation of **BCP1** did not have a significant influence on the T_g of the cured materials within each material system. A decrease could have been expected as the polymeric blocks of **BCP1** consist of short PCL and PDMS blocks for which T_g low as −70 °C resp. −130 °C are known (Koleske et al., 1969; Klonos, 2018). However, since the glass transition temperature of the matrix does not change, **BCP1** must be present in separate, independent structures, as can be assumed due to its self-assembly behavior.

Moreover, the results show that the spacer length of the **DMA** monomer has an influence on the thermomechanical properties of the cured materials. Indeed, the shorter the spacer, the higher the T_g and the storage modulus. Comparing **DMA1**/PEMA to the **DMA3**/PEMA in the neat system, the T_g increases from 87 °C to 105 °C and the storage modulus from 1057 MPa to 1317 MPa. This trend is attributed to the decreasing flexibility of shorter alkyl spacers.

Figs. 7 and 8 show the results from flexural testing in terms of flexural strength and modulus.

Statistical analysis of flexural modulus by one-way ANOVA with post-hoc Tukey's test ($p = 0.05$) revealed a correlation between flexural modulus and spacer length for all formulations containing **BCP1** with higher modulus values observed for shorter spacers. Furthermore, a

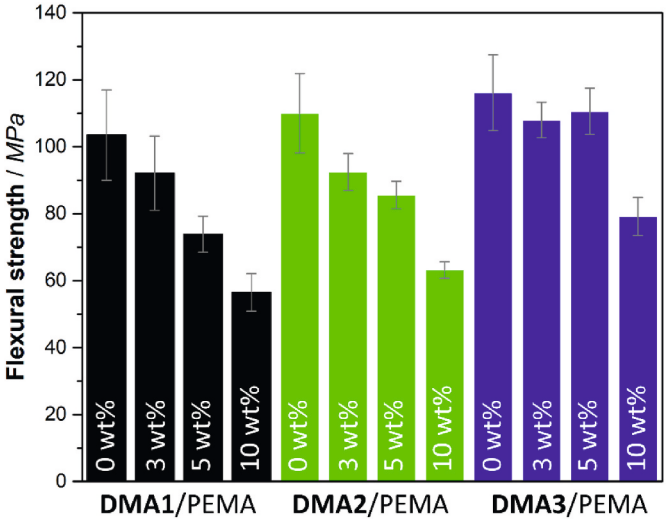

Fig. 7. Flexural strength for **DMAs 1**–**3**/PEMA based materials containing 0, 3, 5 and 10 wt% **BCP1** after 24 h of storage in water at 37 °C.

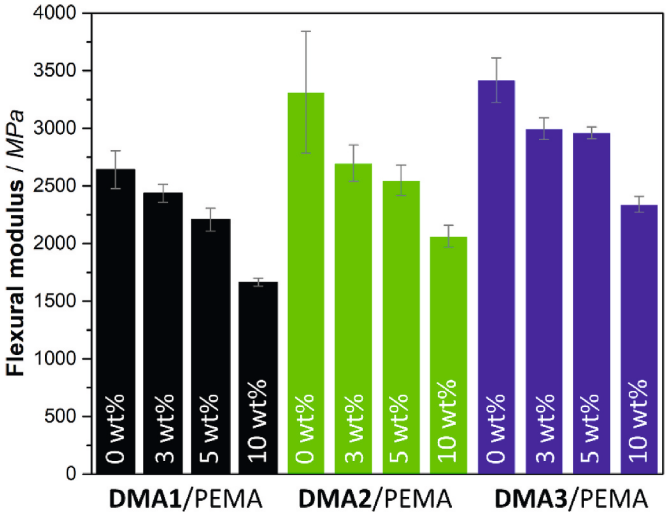

Fig. 8. Flexural modulus for **DMAs 1**–**3**/PEMA based materials containing 0, 3, 5 and 10 wt% **BCP1** after 24 h of storage in water at 37 °C.

correlation was identified between flexural modulus and the concentrations of **BCP1** for each crosslinker **DMA1-3**, with lower modulus observed at higher concentrations of **BCP1**. These findings further support the previously proposed assumptions regarding flexibility and spacer length, as well as the influence of **BCP1** on stiffness. The more detailed results of statistical analysis are available in table SI1 in the supporting information (SI).

3.3. Fracture mechanics and compression testing

The fracture toughness K_{IC} and critical energy release rate G_{IC} of cured **DMAs 1**–**3**/PEMA materials containing various amounts of **BCP1** are presented in Fig. 9 (detailed values are available in table SI2 in the SI).

Regarding the standard **DMA1**/PEMA system, first the addition of **BCP1** to the **DMA1**/PEMA mixture led to a significant increase of both fracture toughness and critical energy release rate. The higher the **BCP1** content, the stronger the increase. Although the neat **DMA1**/PEMA material exhibits a low fracture toughness value of only 0.86 MPa$\sqrt{m}$, the incorporation of 10 wt% **BCP1** leads to a significant increase of 177

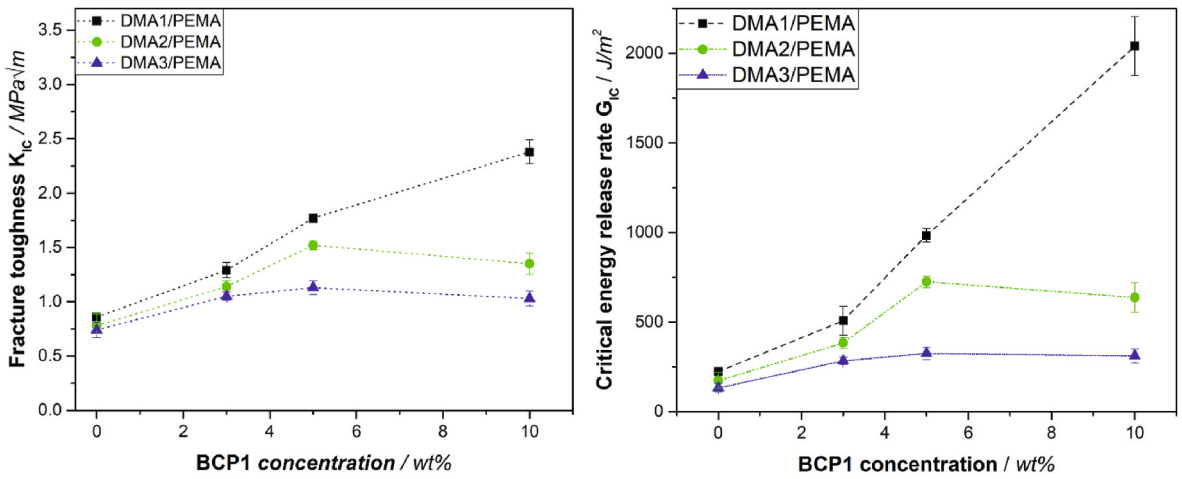

Fig. 9. Fracture toughness K_{IC} and critical energy release rate G_{IC} of the **DMA 1**–**3**/PEMA systems as a function of toughener concentration.

% (K_{IC} = 2.38 MPa$\sqrt{m}$). For **DMA2**/PEMA and **DMA3**/PEMA based materials, the increase of the fracture toughness (K_{IC} and G_{IC}) is less pronounced. Their highest toughness results from addition of 5 wt% of **BCP1**, with a decreasing toughness for 10 wt% **BCP1**. This might be connected to a lowered toughening efficiency of **BCP1** due to the higher crosslink density for the shorter spacers, which limits the maximum toughness for those materials.

For a given **BCP1** content, the following trend could be identified: The longer the spacer group of the urethane macromonomer, the higher the fracture toughness and critical energy release rate.

The presented results demonstrate that the formulation of 3D printable materials consisting of both high fracture toughness and flexural strength and modulus, is challenging. Indeed, the shortening of the urethane dimethacrylate spacer group is beneficial for flexural strength and modulus but detrimental for the fracture toughness of **BCP1**-containing materials. Therefore, a compromise must be found. Here, the formulation **DMA2**/PEMA with 5 wt% **BCP1** exhibits excellent mechanical properties in combination with high fracture toughness and is therefore seen as most promising material.

Additionally, compression testing was performed to get a detailed insight into the influence of the network architecture by means of the alkyl spacer variation within **DMAs 1**–**3**/PEMA systems. The yield stress from compression testing, allows to determine the radius of the plastic zone during the crack propagation of the K_{IC} testing. Fig. 10 shows an overview of the results.

Looking at the yield stresses along **DMAs 1**–**3**/PEMA, there is a clear trend for a decrease in the **BCP1**-free systems due to the systematic increase in chain length. This trend is also observed for **BCP1**-containing materials and is in agreement with the DMTA measurements. The development of the yield stress clearly indicates an increase of the network density due to the reduction of the alkyl chain length.

The previously observed trend that the fracture toughness in **DMA2**/PEMA and **DMA3**/PEMA does not significantly increase for **BCP1** concentrations higher than 5 wt% (or even decreases), is also reflected via the radius of the plastic zone (see Fig. 10). It can be assumed that, due to the reduction of the chain length and thus increased network densities, a threshold is reached at which the formation of the plastic zone is inhibited. Hence, despite higher toughener contents, no further improvement of the fracture toughness can be achieved (detailed values are available in Table SI3 in the SI).

It is important to note that the key findings with regard to thermo-mechanical and mechanical properties as well as fracture mechanics are related to the investigations of the cured bulk materials. For future studies, it is therefore crucial to transfer the knowledge gained to

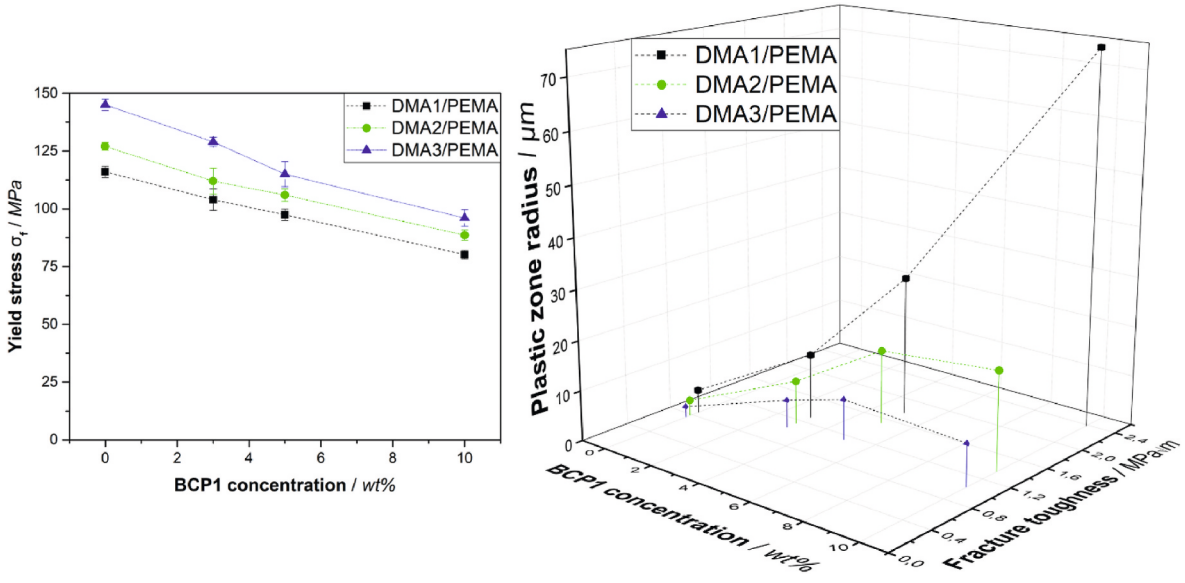

Fig. 10. Compressive yield stress vs. **BCP1** concentration for **DMAs 1**–**3**/PEMA (left) and representation of plastic zone radius vs. K_{IC} values (right).

directly 3D printed samples to ensure that the trends identified are also applicable to relevant products with regard to dental applications.

3.4. Influence of BCP1 on the resin morphology

For understanding the toughening mechanism, fracture surfaces were analyzed by scanning electron microscopy (SEM) (Fig. 11).

A first comparison of the neat systems without **BCP1** shows no initial clear difference in the structure of the fracture surface for all systems. Nevertheless, due to the already intermediate fracture toughness of the initial systems of 0.86 ± 0.02 MPa$\sqrt{m}$ to 0.74 ± 0.07 MPa$\sqrt{m}$, (cf. Table SI2) first plastic deformations are already seen, and no smooth fracture surface of brittle materials is given.

However, first differences in fracture surfaces are evident for a **BCP1** loading of 3.0 wt%. In addition to the classical fracture mechanisms such as shear bands, pull-out and cavitations, differences in the formation of the cavitations are seen. In particular, the systems of **DMA3**/PEMA and **DMA2**/PEMA, e.g., with the specifically adjusted higher network densities, exhibit cavitations of a size of up to 200 nm and more. In the low network density system of **DMA1**/PEMA, the cavitations are significantly smaller. This trend continues even with a further increase in the **BCP1** up to 5 wt%. However, the effect of plastic deformation of the fracture surface increases significantly in the direction of microscale deformation with addition of **BCP1**, as in case of the shorter spacer length of **DMA1**/PEMA. In a preliminary work by Demleitner et al., it was shown that the **BCP1** primarily self-assembles into (spherical) particles with a size of ~20 nm in the system of **DMA1**/PEMA (Demleitner et al., 2022). The significant increase in the size of the cavities along the **DMA2**/PEMA and **DMA3**/PEMA suggests that a too dense network architecture suppresses the uniform formation of the **BCP1** units in the size range of 20 nm and leads to agglomerates of the **BCP1** with dimensions of up to ~200 nm or even more. Revisiting the results of fracture toughness (Fig. 9 and Table SI2), the fracture toughness tends to no longer increase in the more densely arranged networks of **DMA2**/PEMA and **DMA3**/PEMA, or even decreases again with further increase in **BCP1** concentration. This phenomenon may be attributed to the formation of agglomerates and potentially from a reduction of specific surface area between the matrix and the toughener particles, thus lowering the surface interaction between them. Finally, a further difference in the fracture surface at 10 wt% **BCP1** in **DMA1**/-PEMA only becomes apparent from this loading. A similar strong plastic deformation of the fracture surface with the same characteristics as the lower cross-linked systems is only formed at this point. Considering the critical energy release rate G_{IC}, it becomes apparent that significantly more energy is required to generate the critical crack propagation in case of **BCP1** loading. To underline the assumption for the enlargement of the **BCP1** particles or agglomerates in case of an increase of the network density, TEM micrographs have been taken (Fig. 12).

The TEM micrographs show initially no significant differences at the low **BCP1** concentrations of 3 and 5 wt% in **DMAs 1**–**3**/PEMA. The dark spots indicate the **BCP1** particles that have formed, having a size of approximately 20 nm. Only **DMA3**/PEMA, with 10 wt% **BCP1** shows a significantly greater accumulation of domains of **BCP1**. These show an arrangement of small (spherical) particles or elongated structures, which can be described as worm-like. However, there is still an approximate diameter along the worm-like structures of around 20 nm. It is therefore possible that the worm-like structure simply consists of an agglomeration of the spherical particles and is not a true worm-like morphology. It is reasonable to assume that the denser network hinders a fine and homogeneous distribution of the **BCPs**, and therefore leads to significantly more agglomerates.

The PDMS block of the **BCP1**, a PCL-PDMS-PCL triblock copolymer is known to be immiscible in methacrylate-based resins such as **DMAs 1**–**3**/PEMA and is therefore expected to cause a nanophase separation leading to efficient toughening. Demleitner et al. (2022) reported for the systems **DMA1**/PEMA with **BCP1** (**BCP1** 3, 5, 10 wt%, **DMA1**/PEMA 50 wt%/50 wt%) the formation of nano-domains, which had at least in one dimension a size range of about 20 nm. The domains were attributed to the **BCP**, which transform with increasing content from individual units with aspect ratios of ~1 to self-assembled **BCP** clusters with aspect ratios >1. At 5 wt% **BCP** concentration only single core-shell structures or small individual aggregates are expected, but no super-structuring over the whole resin matrix.

To detect morphological changes due to **BCP** incorporation, small

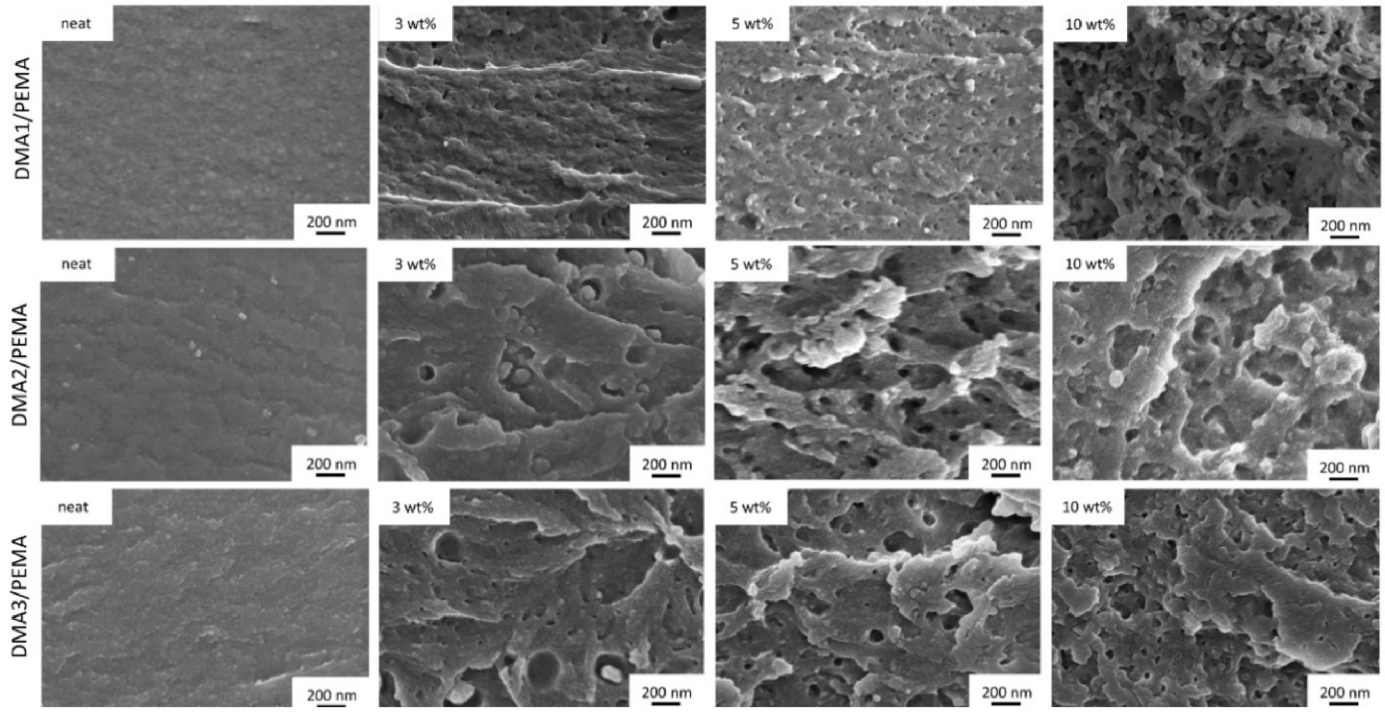

Fig. 11. SEM micrographs of fracture surfaces for the different **DMAs 1**–**3**/PEMA materials.

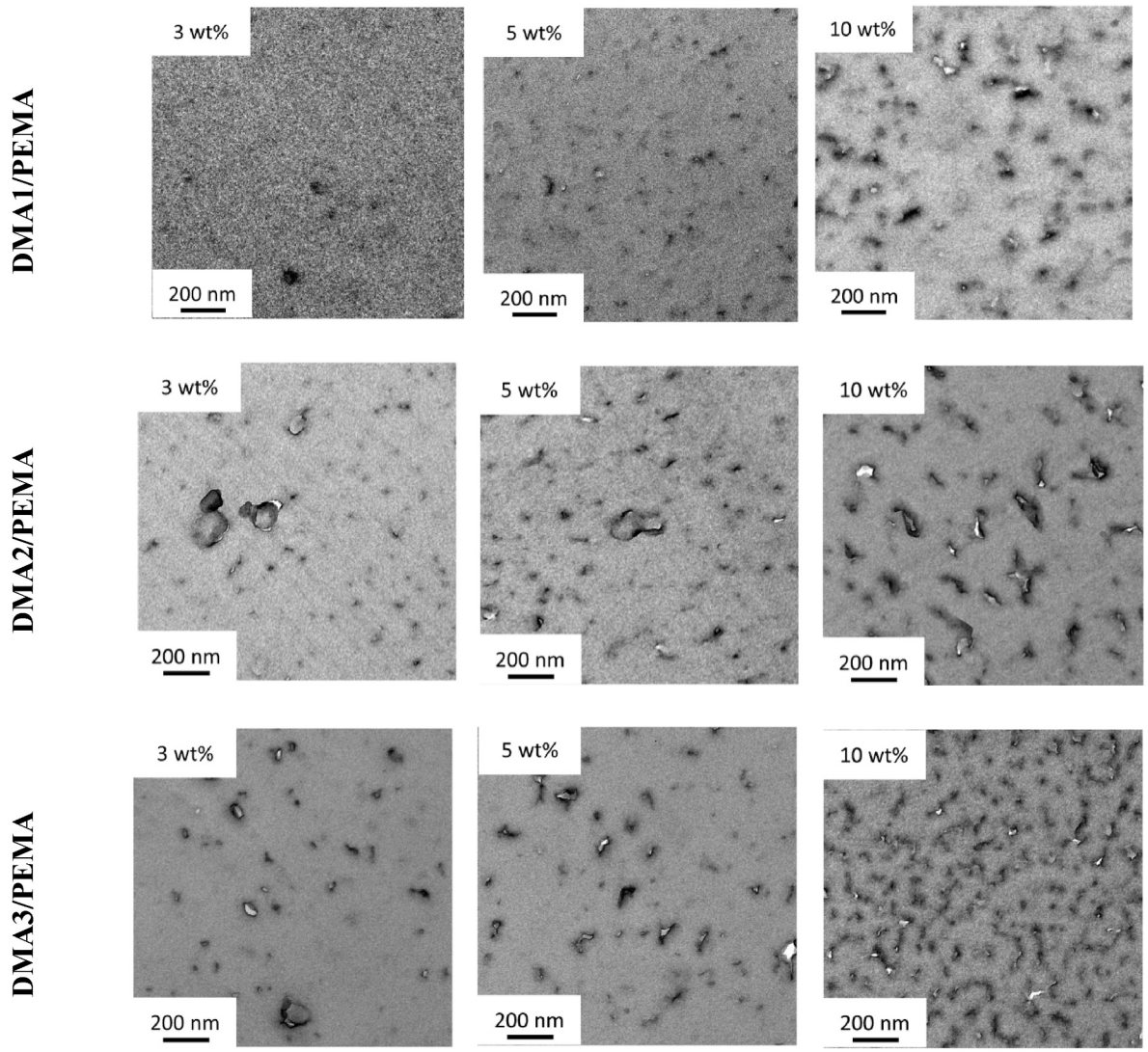

Fig. 12. TEM measurements for the different **DMAs 1**–**3**/PEMA mixtures.

angle X-ray scattering (SAXS) measurements are performed before and after UV-curing. To determine the scattering intensity of **BCP1** alone, the scattering of the corresponding neat systems was subtracted from the scattering of the loaded sample (Fig. 13 and SI: Fig. 1). The 2D SAXS patterns (not shown here) are isotropic, reflecting a homogeneous distribution of the **BCPs**.

The radial averaged intensities differ in region I but are similar in region II. While in region I structural correlations in the size range of $d > \sim 50$ nm (approximation $d = 2\pi/q$) dominate the scattering, the theoretical scattering of individual unit with a radius of gyration of 7.5 nm (solid line), which is in the expected size of a PDMS building (see Demleitner et al. (2022)), describes the experimental data in region II. Thus, with high probability this scattering contribution is caused by the PDMS building blocks. These units still dominate region II, even if the PDMS units transform into nano-domains responsible for phase separation. The underlying **BCP** agglomeration disturbs the originally homogeneous morphology of neat resins (subtracted as background) explaining the deviations in region I from the theoretical intensity, and thereby proofing **BCP** self-assembly. Since the morphology of the samples shows some kind of self-similarity (see Fig. 12) which most probably is caused by long range connectivity or percolation of the **BCPs**, additionally the scattering of a fractal is given for comparison, indicating that the upturn in region I indeed may result from the formation of (worm-like) network structures. However, precautions must be taken since such a simplification is certainly near the limit of validity and the SAXS data is also not sensitive to structural features over ~200 nm in size.

3.5. Fracture toughness via dynamic fatigue crack propagation da/dN

As a final step to investigate the influence of the urethane monomer spacer length on the influence on the toughness behavior, the most promising systems were also subjected to dynamic fatigue crack propagation tests da/dN (Fig. 14). Based on the previous results from the combination of the fracture toughness and the values of the three-point bending tests, **DMAs 1**–**3**/PEMA with a concentration of 5 wt% **BCP1** were investigated.

In agreement with the static K_{IC} tests, the **BCP1**-free systems **DMAs 2**–**3**/PEMA show hardly any differences along the fracture toughness, which is shown by the respective ΔK_{max} values (see Table 2), where ultimate failure occurs in region III of the instable crack propagation. An increase in ΔK_{max} is only observed by increasing the chain length by means of **DMA1**/PEMA. In case of the 5 wt% **BCP1**-containing systems, an increase in ΔKmax values is clearly visible, demonstrating the higher toughening potential of the longer alkyl spacer. In addition, the slope m of the systems in region II according to the Paris and Erdogan law can be

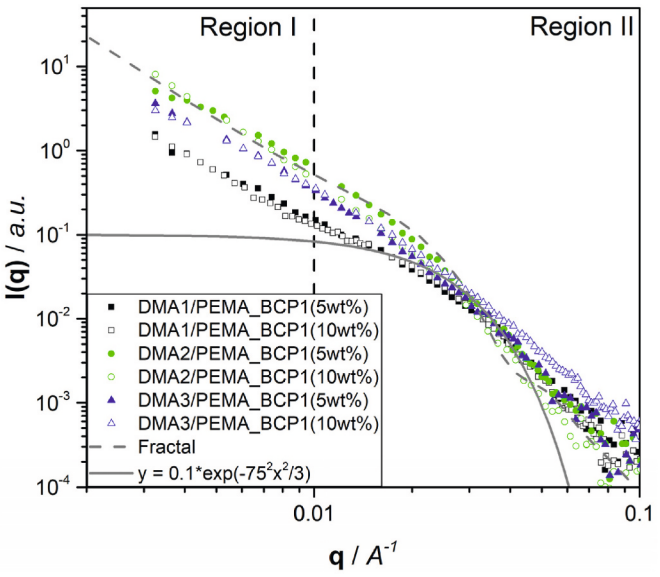

Fig. 13. SAXS data of **BCP1** (filled symbols 5 wt%, open symbols 10 wt%) in **DMAs 1**–**3**/PEMA after UV-curing. For background subtraction the scattering of the corresponding neat sample was used. The samples with 10 wt% **BCP1** are normalized to 5 wt% to show the similarity. Additionally, the theoretical scatterings of individual unit with a radius of gyration of 7.5 nm (solid line) and fractal-like aggregates (dashed line) consisting of spherical building blocks are given (cluster size 200 nm, building block size 10 ± 2 nm, fractal dimension 2.5).

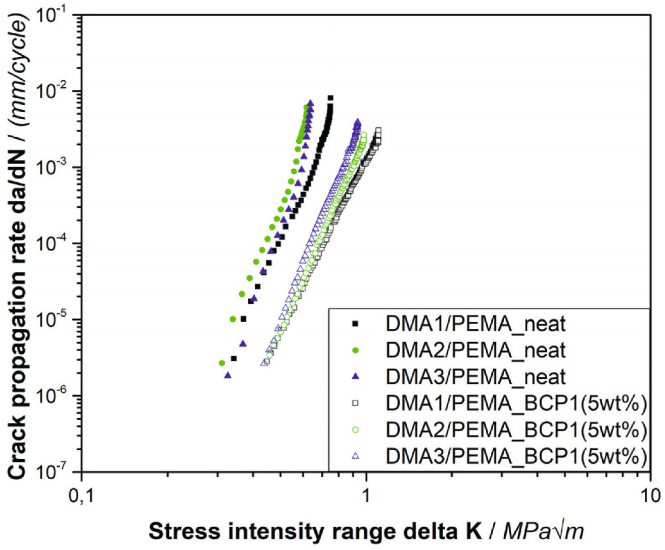

Fig. 14. Fatigue crack propagation testing of **DMAs 1**–**3**/PEMA without and with 5 wt% **BCP1**.

Table 2
Results of the dynamic fatigue crack propagation tests for the **DMA1**/PEMA systems without and with 5 wt% of **BCP1**.

System	BCP1/wt%	Slope m/-	ΔKmax/MPa√m	K_{IC}/MPa√m
DMA1/PEMA	0	7.5	0.75	0.86 ± 0.02
	5	7.4	1.10	1.77 ± 0.04
DMA2/PEMA	0	8.8	0.64	0.78 ± 0.11
	5	8.5	0.98	1.52 ± 0.04
DMA3/PEMA	0	8.8	0.62	0.74 ± 0.07
	5	8.8	0.93	1.13 ± 0.06

observed. The trend to improve the fracture toughness with the modification of the alkyl spacer in terms of an extension of it can also be observed. The longer the alkyl spacer, the lower the slope of stable crack propagation along region II. Although the static K_{IC} values surpass the values from fatigue crack propagation, they show the same trend in terms of the toughening potential. All values are summarized in Table 2.

4. Conclusions

3D printable denture bases must exhibit high fracture toughness as well as high flexural strength and modulus. A compromise must therefore be achieved between toughness and mechanical properties. The nature of the urethane dimethacrylate and the amount of added **BCP** are key parameters to reach the desired objectives of denture bases.

Three urethane dimethacrylates **DMAs 1**–**3** were successfully synthesized. Photo-DSC experiments demonstrated that **DMAs 1**–**3**/PEMA were highly reactive. The final DBC was dependent on the nature of the urethane dimethacrylate. Due to an improved mobility, monomers having a longer spacer group led to higher DBCs. **DMAs 1**–**3** crosslinkers were combined with the monofunctional monomer PEMA, and a PCL-PDMS-PCL triblock copolymer (**BCP1**) was added as toughening agent in various concentrations. For each mixture, the addition of **BCP1** led to a significant increase of fracture toughness due to the presence of nanostructures that formed via self-assembly but reduces the mechanical properties. Cavitation combined with shear yielding present the main toughening mechanisms. It was demonstrated that the nature of the urethane dimethacrylate significantly influences the flexural strength and modulus of the cured material systems as well as the toughening efficiency of the used **BCP1**. The shorter the alkyl spacer, the higher the flexural strength and modulus. On the other hand, materials containing urethane dimethacrylates having short alkyl spacers provided the lowest fracture toughness. This trend is related to the variation of crosslink density of the obtained networks, which influences the T_g and mobility of the chain segments, as well as to the different nature and size of the nanostructures. The **DMA2**/PEMA mixture containing 5 wt% **BCP1** seems to be the ideal choice as a novel material for 3D printed denture bases as it provides a good compromise between high toughness and good flexural properties.

3D printing of this particular formulation will be investigated in the future. The choice of dimethacrylate monomer and **BCP** concentration should be carefully considered to achieve the desired mechanical properties and toughness.

Furthermore, future studies will analyze the influence of the nature of further **BCPs** (like molecular weight, block ratio, etc.) on the toughening ability.

CRediT authorship contribution statement

Florian Schönl: Writing – original draft, Visualization, Investigation, Data curation, Conceptualization. **Martin Demleitner:** Writing – review & editing, Funding acquisition, Conceptualization. **Jörg Angermann:** Investigation. **Pascal Fässler:** Investigation. **Iris Lamparth:** Investigation. **Kai Rist:** Supervision, Resources, Project administration. **Thomas Schnur:** Investigation. **Yohann Catel:** Writing – review & editing, Writing – original draft, Data curation, Conceptualization. **Sabine Rosenfeldt:** Writing – review & editing, Writing – original draft, Investigation, Formal analysis, Data curation. **Holger Ruckdäschel:** Writing – review & editing.

Declaration of competing interest

The authors declare that they have no known competing financial interests or personal relationships that could have appeared to influence the work reported in this paper.

Data availability

Data will be made available on request.

Acknowledgment

This work benefited from the use of the SasView application, originally developed under NSF Award DMR-0520547. SasView also contains code developed with funding from the EU Horizon 2020 programme under the SINE2020 project Grant No 654000.

Funded by the Open Access Publishing Fund of the University of Bayreuth.

Appendix A. Supplementary data

Supplementary data to this article can be found online at https://doi.org/10.1016/j.jmbbm.2024.106737.

References

Aati, S., et al., 2022. Effect of post-curing light exposure time on the physico–mechanical properties and cytotoxicity of 3D-printed denture base material. Dent. Mater. 38, 57–67.

Abou Jaoude, A., 2015. Analytic and linear prognostic model for a vehicle suspension system subject to fatigue. Syst. Sci. Control Eng. 3, 81–98.

Altarazi, A., Haider, J., Alhotan, A., Silikas, N., Devlin, H., 2022. Assessing the physical and mechanical properties of 3D printed acrylic material for denture base application. Dent. Mater. 38, 1841–1854.

Andjela, L., et al., 2022. A review on Vat Photopolymerization 3D-printing processes for dental application. Dent. Mater. 38, e284–e296.

Anseth, K.S., Wang, C.M., Bowman, C.N., 1994. Kinetic evidence of reaction diffusion during the polymerization of multi(meth)acrylate monomers. Macromolecules 27, 650–655.

Anusavice, Kenneth J., Phillips, Ralph W., Shen, C., Rawls, Henry, Phillips, R., 2013. Science of Dental Materials. Elsevier Saunders.

Bagheri, R., Marouf, B.T., Pearson, R.A., 2009. Rubber-toughened epoxies: a critical review. Polym. Rev. 49, 201–225.

Balhaddad, A.A., et al., 2023. Three-dimensional (3D) printing in dental practice: applications, areas of interest, and level of evidence. Clin. Oral Invest. 27, 2465–2481.

Berchtold, K.A., et al., 2004. Novel monovinyl methacrylic monomers containing secondary functionality for ultrarapid polymerization: steady-state evaluation. Macromolecules 37.

Bhushan, B., Burton, Z., 2005. Adhesion and friction properties of polymers in microfluidic devices. Nanotechnology 16, 467–478.

Broek, D., 1982. The crack tip plastic zone. In: Elementary Engineering Fracture Mechanics. Springer Netherlands, pp. 91–114. https://doi.org/10.1007/978-94-009-4333-9_4.

Bucknall, C.B., Dumpleton, P., 1987. Acceleration of FCP in toughened PMMA following a step increase in load amplitude. Int. J. Fatig. 9.

Cai, H., et al., 2023. Dental materials applied to 3D and 4D printing technologies: a review. Polymers 15, 2405.

Cong, H., Li, L., Zheng, S., 2014. Formation of nanostructures in thermosets containing block copolymers: from self-assembly to reaction-induced microphase separation mechanism. Polymer (Guildf). 55, 1190–1201.

Cramer, N.B., O'Brien, C.P., Bowman, C.N., 2008. Mechanisms, polymerization rate scaling, and oxygen inhibition with an ultra-rapid monovinyl urethane acrylate. Polymer (Guildf). 49, 4756–4761.

Dean, J.M., Lipic, P.M., Grubbs, R.B., Cook, R.F., Bates, F.S., 2001. Micellar structure and mechanical properties of block copolymer-modified epoxies. J. Polym. Sci., Part B: Polym. Phys. 39, 2996–3010.

Dean, J.M., Grubbs, R.B., Saad, W., Cook, R.F., Bates, F.S., 2003. Mechanical properties of block copolymer vesicle and micelle modified epoxies. J. Polym. Sci., Part B: Polym. Phys. 41, 2444–2456.

Della Bona, A., Cantelli, V., Britto, V.T., Collares, K.F., Stansbury, J.W., 2021. 3D printing restorative materials using a stereolithographic technique: a systematic review. Dent. Mater. 37, 336–350.

Demleitner, M., et al., 2022. Influence of block copolymer concentration and resin crosslink density on the properties of UV-curable methacrylate resin systems. Macromol. Mater. Eng. 307, 2200320.

Doucet, M., et al., 2019. SasView Version 4.2.2. https://doi.org/10.5281/zenodo.2652477.

Falahchai, M., Ghavami-Lahiji, M., Rasaie, V., Amin, M., Neshandar Asli, H., 2023. Comparison of mechanical properties, surface roughness, and color stability of 3D-printed and conventional heat-polymerizing denture base materials. J. Prosthet. Dent 130, 266.e1–266.e8.

Geiger, V., Mayinger, F., Hoffmann, M., Reymus, M., Stawarczyk, B., 2024. Fracture toughness, work of fracture, flexural strength and elastic modulus of 3D-printed denture base resins in two measurement environments after artificial aging. J. Mech. Behav. Biomed. Mater. 150, 106234.

Grellmann, W., Seilder, S., 2013. Polymer Testing. Car Hanser Verlag GmbH & Co. KG.

Hillmyer, M.A., Lipic, P.M., Hajduk, D.A., Almdal, K., Bates, F.S., 1997. Self-assembly and polymerization of epoxy resin-amphiphilic block copolymer nanocomposites. J. Am. Chem. Soc. 119, 2749–2750.

Hodgkin, J.H., Simon, G.P., Varley, R.J., 1998. Thermoplastic toughening of epoxy resins: a critical review. Polym. Adv. Technol. 9, 3–10.

Hübner, F., et al., 2021. Low temperature fatigue crack propagation in toughened epoxy resins aimed for filament winding of type V composite pressure vessels. Polym. Test. 102, 107323.

Kishi, H., et al., 2015. Control of nanostructures generated in epoxy matrices blended with PMMA-b-PnBA-b-PMMA triblock copolymers. Express Polym. Lett. 9, 23–35.

Klonos, P.A., 2018. Crystallization, glass transition, and molecular dynamics in PDMS of low molecular weights: a calorimetric and dielectric study. Polymer (Guildf). 159, 169–180.

Koleske, J.V., Lundberg, R.D., Lactone polymers, I., 1969. Glass transition temperature of poly-ε-caprolactone by means on compatible polymer mixtures. J. Polym. Sci. 2 Polym. Phys. 7, 795–807.

Kothmann, M., 2017. Einfluss der Nanopartikelgeometrie auf die Bruchzähigkeit und das Ermüdungsverhalten von Epoxidharzen. University of Bayreuth.

Kothmann, M.H., Zeiler, R., Rios de Anda, A., Brückner, A., Altstädt, V., 2015. Fatigue crack propagation behaviour of epoxy resins modified with silica-nanoparticles. Polymer (Guildf). 60, 157–163.

Kothmann, M.H., et al., 2017. Fatigue Crack Growth Behaviour of Epoxy Nanocomposites—Influence of Particle Geometry, pp. 23–32. https://doi.org/10.1007/978-3-319-41879-7_2.

Krishna Alla, R., et al., 2015. Conventional and Contemporary polymers for the fabrication of denture prosthesis: part I-Overview, composition and properties. Int. J. Appl. Decis. Sci. 1.

Ligon-Auer, S.C., Schwentenwein, M., Gorsche, C., Stampfl, J., Liska, R., 2016. Toughening of photo-curable polymer networks: a review. Polym. Chem. 7, 257–286.

Lipic, P.M., Bates, F.S., Hillmyer, M.A., 1998. Nanostructured thermosets from self-assembled amphiphilic block copolymer/epoxy resin mixtures. J. Am. Chem. Soc. 120, 8963–8970.

Meng, F., Zheng, S., Li, H., Liang, Q., Liu, T., 2006a. Formation of ordered nanostructures in epoxy thermosets: a mechanism of reactin-induced microphase separation. Macromolecules 39, 5072–5080.

Meng, F., Zheng, S., Zhang, W., Li, H., Liang, Q., 2006b. Nanostructured thermosetting blends of epoxy resin and amphiphilic poly(ε-caprolactone)- b lock -polybutadiene- b lock -poly(ε-caprolactone) triblock copolymer. Macromolecules 39, 711–719.

Mi, X., et al., 2022. Toughness and its mechanisms in epoxy resins. Prog. Mater. Sci. 130, 100977.

Mishra, K., Pandey, G., Singh, R.P., 2017. Enhancing the mechanical properties of an epoxy resin using polyhedral oligomeric silsesquioxane (POSS) as nano-reinforcement. Polym. Test. 62, 210–218.

Mousavi, S.R., et al., 2021. Toughening of epoxy resin systems using core–shell rubber particles: a literature review. J. Mater. Sci. 56, 18345–18367.

Punia, U., Kaushik, A., Garg, R.K., Chhabra, D., Sharma, A., 2022. 3D printable biomaterials for dental restoration: a systematic review. Mater. Today Proc. 63, 566–572.

Redline, E.M., Francis, L.F., Bates, F.S., 2011. Radical-cured block copolymer-modified thermosets. J. Polym. Sci., Part B: Polym. Phys. 49, 540–550.

Ritzenthaler, S., et al., 2002. ABC triblock copolymers/Epoxy−Diamine blends. 1. Keys to achieve nanostructured thermosets. Macromolecules 35, 6245–6254.

Roshanali, M., Nodehi, A., Atai, M., 2020. Synthesis and characterization of core-shell nanoparticles and their application in dental resins. J. Mech. Behav. Biomed. Mater. 110, 103926.

Ruckdäschel, H., et al., 2007. Toughening of immiscible PPE/SAN blends by triblock terpolymers. Polymer (Guildf). 48, 2700–2719.

Ruckdäschel, H., Fischer, F., Altstädt, V., Müller, A.H.E., 2008. Fatigue crack growth behavior of multiphase blends. J. Solid Mech. Mater. Eng. 2, 417–427.

Ruiz-Pérez, L., Royston, G.J., Fairclough, J.P.A., Ryan, A.J., 2008. Toughening by nanostructure. Polymer (Guildf). 49, 4475–4488.

Sandmann, B., et al., 2015. Incorporation of core–shell particles into methacrylate based composites for improvement of the mechanical properties. Polym. Chem. 6, 5273–5280.

Santiago, D., Serra, À., 2022. Enhancement of epoxy thermosets with hyperbranched and multiarm star polymers: a review. Polymers 14, 2228.

Shah, M.B., Ferracane, J.L., Kruzic, J.J., 2009. Mechanistic aspects of fatigue crack growth behavior in resin based dental restorative composites. Dent. Mater. 25, 909–916.

Sprenger, S., 2020. Nanosilica-toughened epoxy resins. Polymers 12, 1777.
Thompson, Z.J., et al., 2009. Block copolymer toughened epoxy: role of cross-link density. Macromolecules 42, 2333–2335.
Tigmeanu, C.V., Ardelean, L.C., Rusu, L.-C., Negrutiu, M.-L., 2022. Additive manufactured polymers in dentistry, current state-of-the-art and future perspectives-A review. Polymers 14, 3658.
Utaloff, K., et al., 2019. Improvement of fracture toughness and glass transition temperature of DGEBA based epoxy-systems using toughening and crosslinking modifiers. Polym. Eng. Sci. 59, 86–95.
Wang, J., Zhang, X., Jiang, L., Qiao, J., 2019. Advances in toughened polymer materials by structured rubber particles. Prog. Polym. Sci. 98, 101160.
Wu, J., Thio, Y.S., Bates, F.S., 2005. Structure and properties of PBO–PEO diblock copolymer modified epoxy. J. Polym. Sci., Part B: Polym. Phys. 43, 1950–1965.
Xu, Q., Zhou, Q., Shen, K., Jiang, D., Ni, L., 2016. Nanostructured epoxy thermoset templated by an amphiphilic PCL- b -PES- b -PCL triblock copolymer. J. Polym. Sci., Part B: Polym. Phys. 54, 424–432.
Zappini, G., Kammann, A., Wachter, W., 2003. Comparison of fracture tests of denture base materials. J. Prosthet. Dent 90, 578–585.